Semiconductor Lasers: Device Physics and Applications

Academic and Research Staff

Professor Rajeev J. Ram, Holger Schmidt

Graduate Students

Mathew C. Abraham, Song-Ho Cho, George Cragg, Harry L. T. Lee , Tom Liptay, Peter Mayer, Kevin P. Pipe , Farhan Rana , Margaret Wang

Abstract
The Semiconductor Laser Group within RLE addresses science and technology questions that arise during the development and application of new device technologies. During the last year the research results from the group have included:

- Models for noise in various semiconductor lasers were developed. The devices studied included:
    - Surface emitting lasers
    - Quantum cascade lasers
    - Mode-locked semiconductor lasers.
- Experimental facilities for measuring noise were developed. These included the fabrication of a test station for measuring noise at low frequency (<100 kHz) in both high and low impedance devices and at high frequency (<18 GHz). These new test stations are being used to study current noise in quantum cascade lasers. In addition to noise measurements under DC operation, a 12 Gb/s bit error rate tester (BERT) was installed and used to test the noise models for surface emitting lasers.
- Heterojunction thermoelectric cooling was investigated in bipolar devices. The first models for Seebeck and Peltier coefficients in a bipolar device were developed. In addition a test station for microthermal measurements was fabricated and used to study the thermal performance of GaAs and GaSb lasers.
- New models of atomic force and magnetic force microscopy were developed. These models are being used to investigate the sensitivity limits of magnetic force microscopy in imaging electron transport in semiconductor devices.
- A low-temperature (4K) scanning probe microscope facility has been built. This single microscope has been used for scanning tunneling, contact atomic force microscopy and non-contact atomic force microscopy.

High Fidelity Multimode VCSEL Links

Sponsor
Office of Naval Research

Project Staff
Harry L. T. Lee, Professor Rajeev J. Ram
Sandia National Labs: Kent Choquette

In previous work, using multimode vertical cavity surface emitting lasers (VCSELs) for high fidelity RF photonic links was shown to be feasible for applications requiring modest (95-100dB-Hz$^{2/3}$) dynamic range [1]. Experimental measurements revealed an optimal range of DC bias current and RF modulation frequency where the dynamic range was highest. This was due to an increase in the noise floor and higher than expected distortion at low frequencies and resonant distortion at high frequencies. Because the standard lumped, single mode laser model is not consistent with measurements at low frequencies it is not sufficient to use it as a tool to understand the role of multimode dynamics on device performance. For this reason, a spatially inhomogeneous, multimode, dynamic VCSELs model has been developed and has led to an improved understanding of the role of multiple mode coupling in mode partition noise and nonlinear distortions in multimode VCSELs.

In the model, a cylindrically symmetric geometry is assumed for simplicity and space is discretized by calculating average values of the carrier density over annular rings spanning the VCSEL active area. The different carrier density nodes are coupled through diffusion and stimulated emission of the lasing modes. For a given injection current, the steady state mode powers and carrier densities are calculated and then a small signal perturbation around the steady state operating point are developed which allows a noise and distortion analysis.

The primary results of the modeling are that there is a fast and a slow time scale in multi-transverse mode VCSEL dynamics. In the fast time scale, the carrier density responds to perturbations and positively correlates the perturbations of the lasing modes (Fig. 1 top, Fig. 2.) In this regime, the laser behaves like a single mode laser and the standard lumped, single mode laser model applies, with effective single mode parameters. The influence of multiple modes on the dynamics occurs on the slow time scale where the overall carrier density and total field intensity has approached steady state, while the intermode distribution of energy between multiple modes continues to evolve. These slow intermode dynamics are anti-correlated (Fig. 1 bottom, Fig. 2) and governed by the spontaneous emission rates into the modes and their degree of spatial overlap and influences both the intensity noise and nonlinear distortion properties of multimode VCSELs.

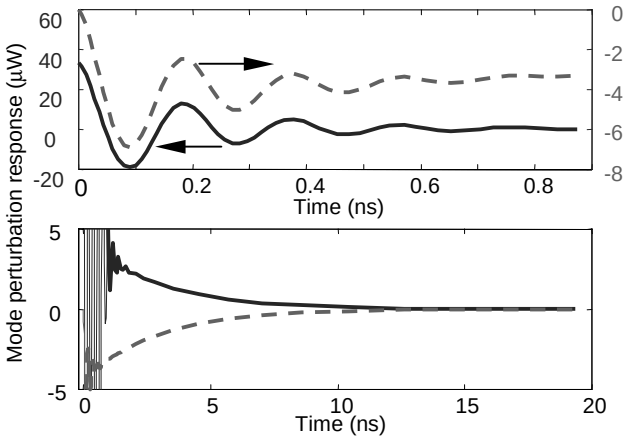

Fig. 1. Time domain perturbation response from a single node, two mode model representing strongly coupled modes where the main mode is increased by 10% at t=0. The main (solid) and side (dashed) mode responses are positively correlated at short times while the total photon density equilibrates and are negatively correlated at long time scales while the individual modes equilibrate.

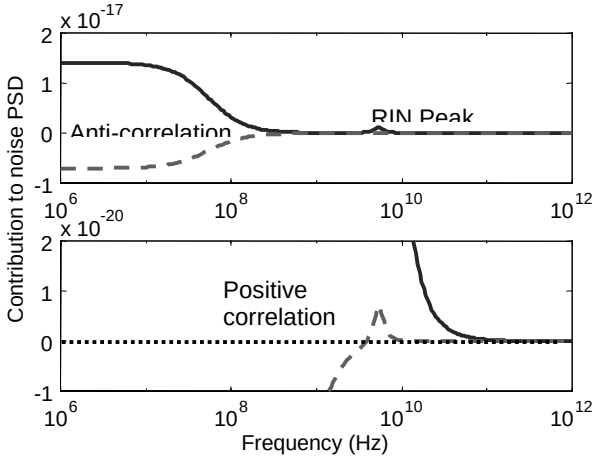

Fig. 2. Main mode autocorrelation (solid) and cross-correlation (dashed) contributions to the noise PSD. In the top plot, the anti-correlation between the main and side mode is indicated by the negative cross-correlation. In the bottom plot, the y-axis is scaled to show the positive cross correlation at the relaxation oscillation frequency.

The low frequency intensity noise is of particular interest because it was shown to limit the maximum dynamic range of RF photonic links. One mechanism responsible for the increase in low frequency intensity noise that is intrinsic to multimode lasers is mode partition noise, which occurs when the power of the different modes is not collected equally, thereby introducing mode selective loss. In VCSELs, where the multiple modes are transverse rather than longitudinal, as in most edge emitting lasers, mode selective loss is easily introduced upon coupling into optical fiber and hence, the low frequency intensity noise in links using such lasers is high. Previous work in this field has focused on the quantum correlations between the modes and the possibility of squeezing the total field intensity [2,3]. In our work, we are more concerned with the spectrum of the intensity noise for different mode selective loss and its physical origin.

There are two different regimes of mode coupling with distinct noise PSD characteristics. The first is common to longitudinal mode lasers where the modes are strongly coupled. In this case, the low frequency noise has a single pole roll off, where the corner frequency is governed by the spontaneous emission rate into the mode. The single pole response arises because the modes are strongly coupled and are mutually over damped. For the case of weak intermode coupling as with transverse modes with limited spatial overlap, the intermode coupling can become slightly decoupled and hence, under damped, showing oscillations. This leads to a noise power spectral density with a second peak at the intermodal oscillation frequency, which is lower than the relaxation oscillation resonance (Fig. 3.) Understanding the type of coupling and the influence on the noise power spectral density is important because under damped intermodal coupling can add a resonant noise peak in a frequency range of interest. Analytical expressions are being developed for simple cases to provide insight for design issues related to multiple mode laser links.

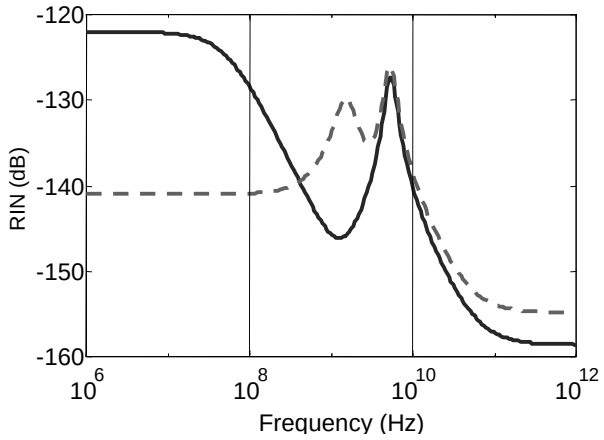

Fig. 3. Calculated relative intensity noise spectra for single node (solid, SMSR = 18dB) and 32 node finite difference (dashed, SMSR = 6dB) model with 50% MSL of the side mode.

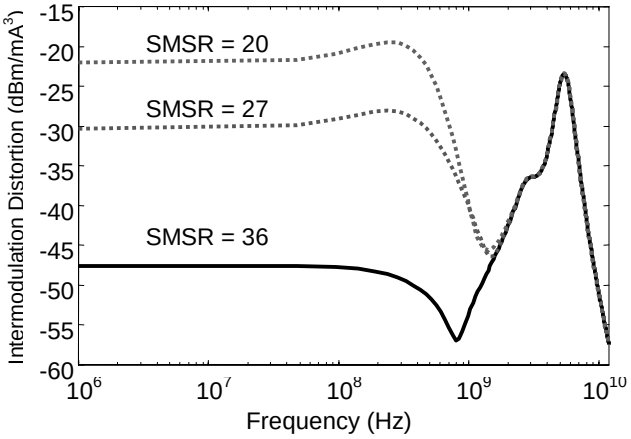

Fig. 4. Intermodulation distortion for a two mode VCSEL structure with different side mode suppression ratio. The weak side mode drives the nonlinear distortion in the main mode at low frequencies where intermode dynamics is important.

The role of multiple modes on the distortion properties of multimode lasers can be understood by considering the origin of the nonlinear distortions. Semiconductor lasers can be modulated linearly for analog applications because the strong negative feedback of the field intensity on the modal gain stabilizes the carrier density at the threshold value and linearizes the stimulated emission contribution to the dynamics. This condition is usually referred to as gain clamping. When the laser is modulated at high speeds or at low field intensity, the strength of the gain clamping is reduced and leads to increased nonlinear distortions. In a multiple mode laser, the local gain clamping is related to the local field intensity. In multimode lasers with non-uniform total field intensity, the increased distortion of weakly

lasing modes can be coupled to the dominant lasing mode over the slow timescale related to the intermodal coupling, leading to greatly increased distortions at low frequencies (Fig. 4) This effect explains the increased observed low frequency distortion and also can provide a side mode suppression ratio guideline for designing single mode devices for RF photonic links.

[1] H. L. T. Lee, R. V. Dalal, R. J. Ram, and K. D. Choquette, "Dynamic range of vertical-cavity surface-emitting lasers in multimode links," *IEEE Photon.Techno. Lett.*, Vol. 11, No. 11 , pp. 1473-1475, Nov. 1999.

[2] G. P. Agrawal, "Mode-partition noise and intensity correlation in a two-mode semiconductor laser," *Phys. Rev. A*, vol. 37, no. 7, pp. 2488-2494, Apr. 1988.

[3] S. Lathi and Y. Yamamoto, "Influence of nonlinear gain and loss on the intensity noise of a multimode semiconductor laser," *Phys. Rev. A*, vol. 59, no. 1, pp. 819-825, Jan. 1999.

Internal Cooling in Semiconductor Diode Lasers

Sponsor
MIT Lincoln Laboratory

Project Staff
Kevin Pipe, Professor Rajeev Ram
UC Santa Cruz: Professor Ali Shakouri

Heat management can be a critical issue in semiconductor diode laser design due to the strong temperature dependencies of threshold current, quantum efficiency, and device lifetime. In WDM systems, wavelength drift caused by temperature fluctuation can generate crosstalk and intensity noise.

Conventional methods for temperature stabilization typically involve an external Peltier cooler placed in the vicinity of the device. Recent efforts aimed at a solution more amenable to integration have led to the consideration of thermoelectric and thermionic effects in thin films. A novel laser design termed the Injection Current Internally Cooled Light Emitter (ICICLE) has been proposed that takes advantage of thermoelectric heat exchange at the junctions between the constituent layers of the device itself to optimize cooling near the active region.

A model has been developed to calculate the thermoelectric heat exchange distribution in a device using self-consistent drift-diffusion / Poisson equations. This model can likewise simulate other heating terms such as Joule heating and non-radiative recombination. The calculated distribution of heating and cooling sources can then be used to calculate heat flow within the device, which can be experimentally verified with a surface-scanning microthermocouple or with a photothermal reflectance measurement.

Band structures under bias and associated thermoelectric terms are shown in Figure 5 for both a conventional SCH laser and an ICICLE. In the conventional design,

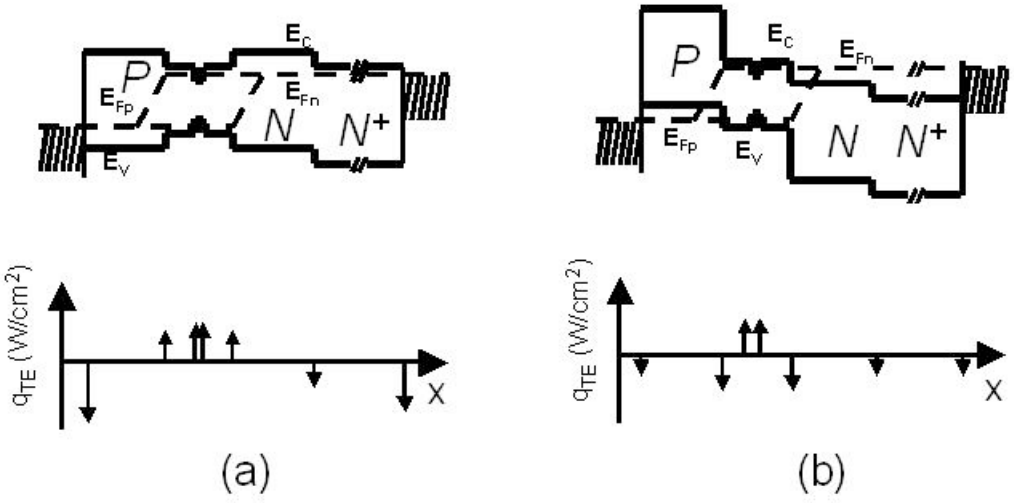

Fig. 5. Band structure and thermoelectric heat exchange for (a) conventional SCH and (b) ICICLE

carriers injected into the core region lose energy through thermoelectric heating at the core/cladding interface, whereas in the ICICLE, injection current causes cooling. Notice that the ICICLE design moves the cooling terms near to the active region and the heating terms away to the edges of the device where heat is more readily conducted away. As long as carrier transport is kept in the diffusive rather than thermionic regime, threshold currents for the two devices are similar.

The staircase ICICLE band alignment can be achieved through the use of either increased cladding doping or Type-II interfaces (such as those found in the GaInAsSb material system). Figure 6 shows both conventional SCH and ICICLE GaInAsSb designs,

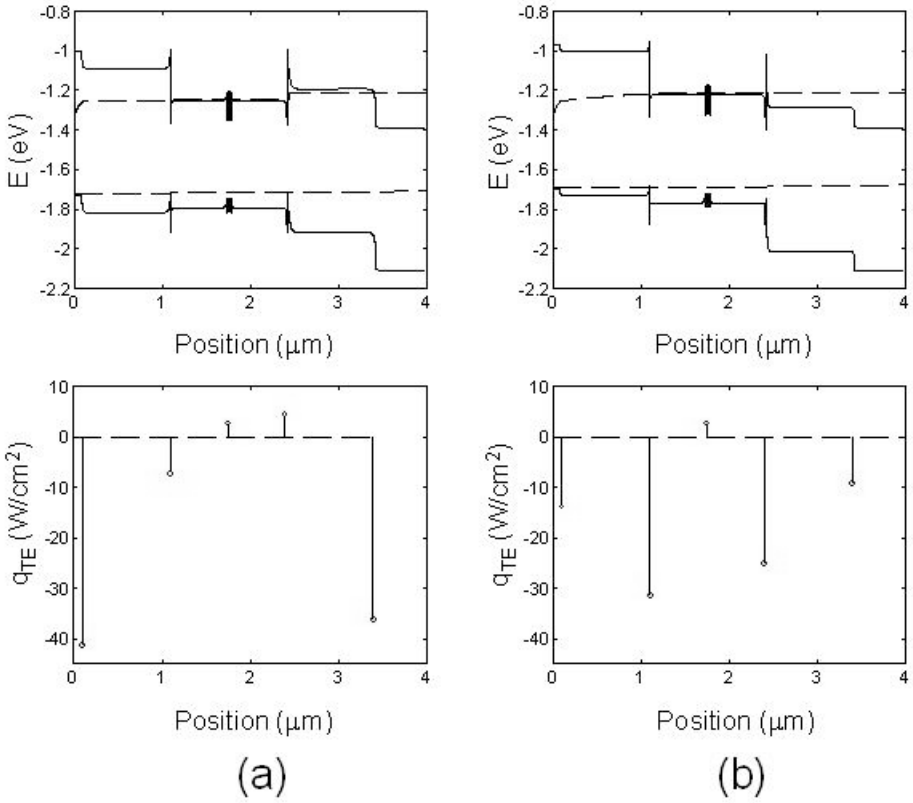

Fig. 6. Band structure and thermoelectric heat exchange at 475 A/cm^2 modeled for (a) conventional SCH (cladding doped at 10^{17}) and (b) ICICLE (cladding doped at 10^{18}) in the GaInAsSb material system.

biased at identical current levels. After modeling carrier transport in the GaInAsSb ICICLE, bipolar double heterostructures were proposed and subsequently grown at Lincoln Laboratory for testing purposes. Unipolar structures were also later proposed for the purposes of demonstrating cooling and further characterizing the material system.

Noise and Timing Jitter in Active and Hybrid Mode-Locked Semiconductor Lasers

Sponsors
Defense Advanced Research Projects Agency – PACT Program

Project Staff
Farhan Rana, Professor Rajeev J. Ram

Active and hybrid mode-locked semiconductor lasers have produced sub-picosecond optical pulses [1]. Short pulse generation from mode-locked semiconductor lasers has important applications in electro-optic sampling, optical analog-to-digital conversion, optical communication systems, and ultra-fast optical measurements. Low noise performance of mode-locked lasers, specially reduced timing jitter, is critical to most of these applications.

We have formulated a comprehensive model for the noise in active and hybrid mode-locked semiconductor lasers. The model includes the effects of gain dispersion, carrier density and accompanying refractive index fluctuations, dynamic gain and loss saturation, and the laser α-parameter on the amplitude, phase, frequency, and the timing fluctuations of mode-locked laser pulses. Noise contributions from spontaneous emission, photon loss, carrier generation and recombination, and from the jitter in the RF drive are included in the model. The model is completely self-consistent, and to the authors' knowledge, a first detailed presentation of the relative contribution of various noise sources to the noise in the mode-locked pulses. Previous noise theories have neglected most of the dynamic effects which are important in semiconductor lasers [2,3].

We derive a master equation for mode-locked laser pulses which, in the presence of gain and loss saturation, dispersion, and non-zero α-parameter, closely resembles the non-linear Hartree-Fock equations of condensed matter physics [2,4]. The master equation is complex and non-Hermitian. It can be solved numerically as a self-consistent eigen-value equation to obtain the laser pulses in the steady state. Perturbation theory for the fluctuations around the steady state is developed by using the eigen-functions of the adjoint master equation. We obtain Langevin equations for the fluctuations in the pulse amplitude, phase, frequency, timing, and the carrier density.

We find that the laser α-parameter is not responsible for converting the carrier density fluctuations into the pulse timing jitter. Group velocity fluctuations induced by the carrier density fluctuations are not described by the α-parameter. Other than the group velocity fluctuations, dynamic gain saturation can also convert the carrier density fluctuations into the pulse timing jitter. However, these two effects give opposite contributions to the timing jitter. Pulse amplitude fluctuations also contribute to the pulse timing and frequency fluctuations because of dynamic saturation of the complex gain. Frequency fluctuations are converted into the timing jitter in the presence of dispersion and/or a non-zero α-parameter. Pulse amplitude fluctuations and the carrier density fluctuations are negatively correlated, and this negative correlation must be taken into account when computing the timing jitter.

Fig. 7 shows the steady state laser pulse in an external cavity 5.6 GHz repetition rate actively mode-locked semiconductor laser. Because of dynamic gain saturation the pulse shape is completely determined by the self-consistent time dependent gain. Fig. 8 shows the various contributions to the spectral density of the timing jitter. The RF drive is assumed to have an RMS jitter of 50 fs in a 10 KHz bandwidth. The contributions from the carrier density and the amplitude fluctuations to the timing jitter spectral density show a relaxation oscillation peak that is heavily damped by the action of the modulator. Fig. 9 shows the contributions to the timing jitter for different pulse energies. For smaller pulse energies the contribution from the carrier density fluctuations is dominated by the carrier density induced fluctuations in the group velocity. The calculations agree well with the experimental measurement of 65 fs intrinsic RMS jitter for a similar laser structure in Ref.[5] shown by the square box in Fig.9.

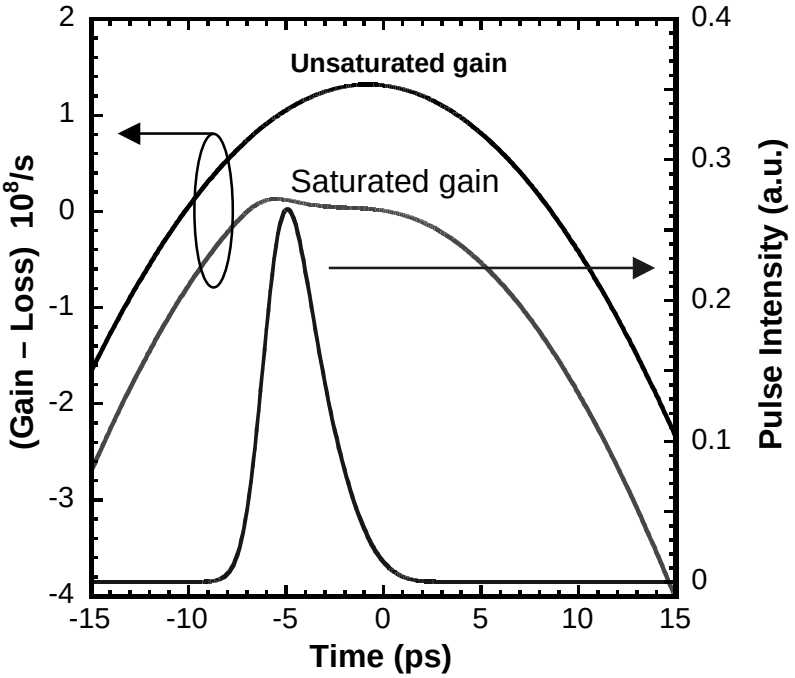

Fig. 7: Self-consistent 0.1 pJ pulse in a 5.6 GHz external cavity actively mode-locked semiconductor laser. The pulse shape and position is determined by the dynamically saturated gain.

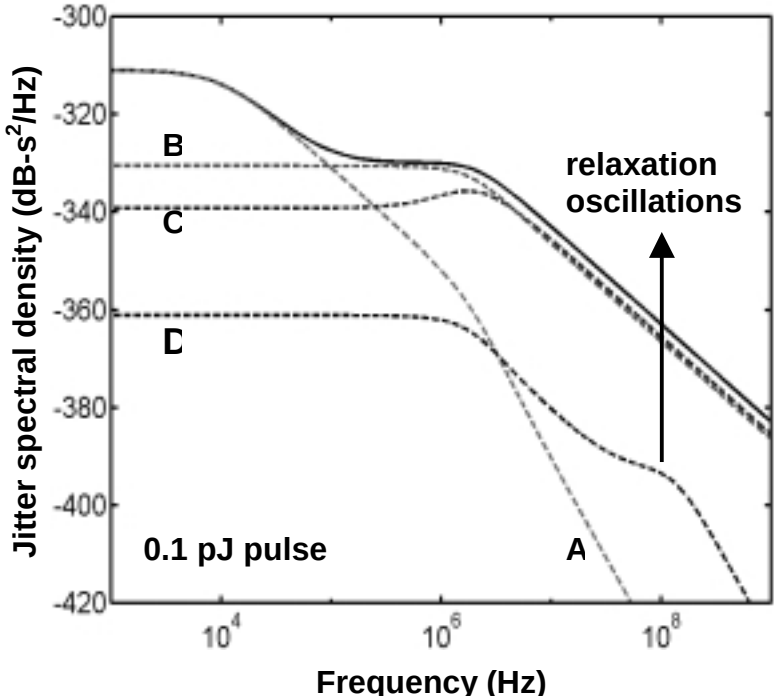

Fig. 8: Contributions to the spectral density of the timing jitter in a 5.6 GHz actively mode-locked semiconductor laser. Solid line is the total timing jitter. **A** is the contribution from the phase noise in the RF drive. **B** is the direct contribution from spontaneous emission noise and photon loss (or vaccum field fluctuations). **C** is the contribution from the frequency noise. **D** is the contribution from the amplitude fluctuations and the carrier density fluctuations.

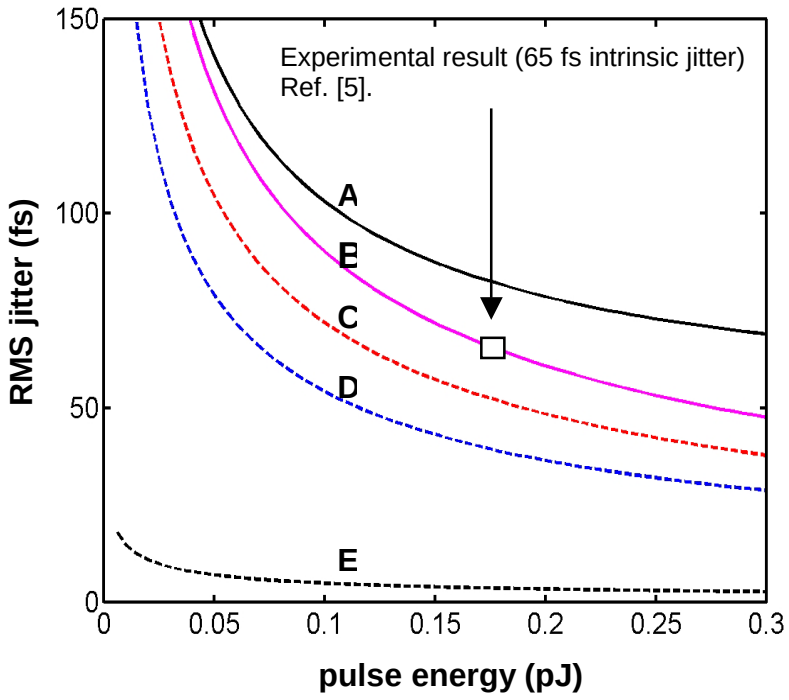

Fig. 9: Contributions to the RMS timing jitter in a 5.6 GHz external actively mode-locked semiconductor laser. **A** is the total RMS timing jitter. **B** is the total intrinsic jitter. **C** is the direct contribution from spontaneous emission noise and photon loss (or vaccum field fluctuations). **D** is the contribution from the frequency noise. **E** is the contribution from the amplitude fluctuations and the carrier density fluctuations. Jitter in the RF drive is assumed to be 50 fs in 10 KHz bandwidth.

References

1. D. J. Derickson, R. J. Helkey, A. Mar, J. R. Karin, J. G. Wasserbauer, J. Bowers, "Short pulse generation using multisegment mode-locked semiconductor lasers," IEEE J. Quantum Electronics, **28,** 2186-2201 (1992).
2. H. A. Haus, A. Mecozzi, "Noise of mode-locked lasers," IEEE J. Quantum Electronics, **29,** 983-996 (1993).
3. D. R. Hjelme, A. R. Mickelson, "Theory of timing jitter in actively mode-locked lasers," IEEE J. Quantum Electronics, **28,** 1594-1606 (1992).
4. A. L. Fetter, J. D. Walecka, "Quantum theory of many particle systems," McGraw Hill, New York, 1971.
5. D. J. Derickson, P. A. Morton, J. E. Bowers, "Comparison of timing jitter in external and monolithic mode-locked semiconductor lasers," Appl. Phs. Lett., **59,** 3372-3374 (1991).

Current Noise, Photon Number Fluctuations and Squeezing in Quantum Cascade Lasers

Sponsors
Office of Naval Research

Project Staff
Farhan Rana, Peter Mayer, Rajeev Ram

Unipolar quantum cascade lasers (**QCL**s) utilizing intersubband transitions to generate photons have become important sources of light in the mid-infrared region (~ 5 μm – 10 μm) [1-4]. The primary application of coherent sources at these wavelengths is spectroscopy. For such applications it is important to quantify the photon noise in **QCL**s. A comprehensive model for the photon number fluctuations in **QCL**s is developed for the first time.

QCLs are different from other interband semiconductor lasers in three important ways which have a significant impact on their noise properties. Firstly, electron transport in **QCL**s takes place by tunneling between states in adjacent quantum wells. It is well known that coulomb interactions in resonant tunneling quantum well structures can suppress (or enhance) current noise by providing a negative (or positive) feedback [5-6]. High impedance suppression of current noise in interband semiconductor lasers can lead to squeezed photon output [7]. It is therefore intriguing whether coulomb correlations in electron transport can also lead to squeezing in **QCL**s. Any model for the photon noise in **QCL**s must take into account these coulomb correlations self-consistently. Secondly, in interband semiconductor lasers the carrier density does not increase beyond its threshold value and, therefore, the noise associated with the non-radiative recombination and generation processes remains unchanged beyond threshold. In **QCL**s the carrier populations in the upper and lower lasing states are not clamped but keep increasing when bias current is increased beyond threshold. Therefore, non-radiative recombination and generation processes contribute significantly to photon noise even at high current biases. Lastly, since all gain sections in a **QCL** are connected electrically and optically, carrier population fluctuations and photon emission events in different gain sections become correlated. It is also the aim of this work to investigate the degree of this correlation and its effect on the photon noise.

The model developed consists of a set of coupled self-consistent Langevin rate equations for fluctuations in carrier populations in different energy levels of a gain stage. Fluctuations in the carrier population are caused by radiative and non-radiative scattering processes, electron tunneling processes and by fluctuations in the current injected into the gain stage. The description of noise associated with electron tunneling by Langevin sources remains valid irrespective of whether the electron transport is coherent or incoherent [5-6]. Photon density fluctuations are also modeled by Langevin rate equations. The Langevin equations describing population fluctuations in different gain stages are coupled since the quantum wells are all coupled to the photon density fluctuations in the same optical cavity and also to the same current fluctuations, which flow through all the gain stages connected in series. Fluctuations in the current are a relaxational response to electron scattering and tunneling events occurring inside all the gain stages of the laser. They are also caused by sources external to the laser which include thermal noise sources associated with circuit resistances. The system of equations obtained this way can easily be solved numerically to give the spectral density of the photon number fluctuations and the current fluctuations.

Numerical results for a 25 stage **QCL** operating at 5 μm are presented here. The details of the structure are reported in reference [2]. We find that the circuit model shown in the inset in Fig. 10, in which current noise sources are attached in parallel with each gain stage, can be used to describe the current noise in **QCL**s. Since the carrier populations in different gain stages interact with photons in the same optical cavity, current noise sources belonging to different gain stages become positively correlated. The current noise from each noise source is found to be suppressed below the shot noise level because of electronic correlations (see Fig. 10). The current noise spectral density (shown in Fig. 11) in the external circuit is found to roll over at the frequency equal to the 3 dB frequency of the laser current modulation response. Therefore, the modulation bandwidth of **QCL**s can be measured by measuring the current noise spectral density. Fig. 12 shows the calculated low frequency Fano Factor of the laser as a function of the bias with and without a 50 Ω series resistor at 300 K. In the absence of the series resistor, the noise is above the shot noise limit, and approaches it asymptotically at high bias. The noise is reduced in the presence of the series resistor. Amplitude squeezing is observed when the bias current increases beyond five times the threshold value. However, the amount of squeezing is negligible being less than 0.25 dB even at extremely high current biases of ten times the threshold value. The two main reasons for the absence of squeezing in **QCL**s have been found to be 1) low differential quantum efficiency, and 2) the fact that carrier density and, therefore, the noise associated with non-radiative processes are not clamped above threshold.

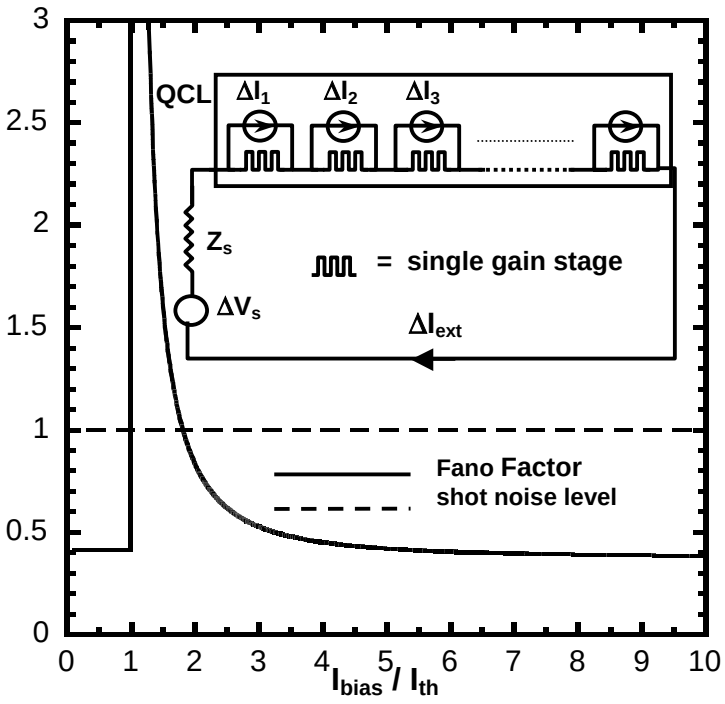

Fig.10: Calculated Fano Factor of the current noise source ΔI is plotted as a function of the bias current. The current noise is suppressed below the shot noise level because of electronic **correlations (device described in ref. [2]).**

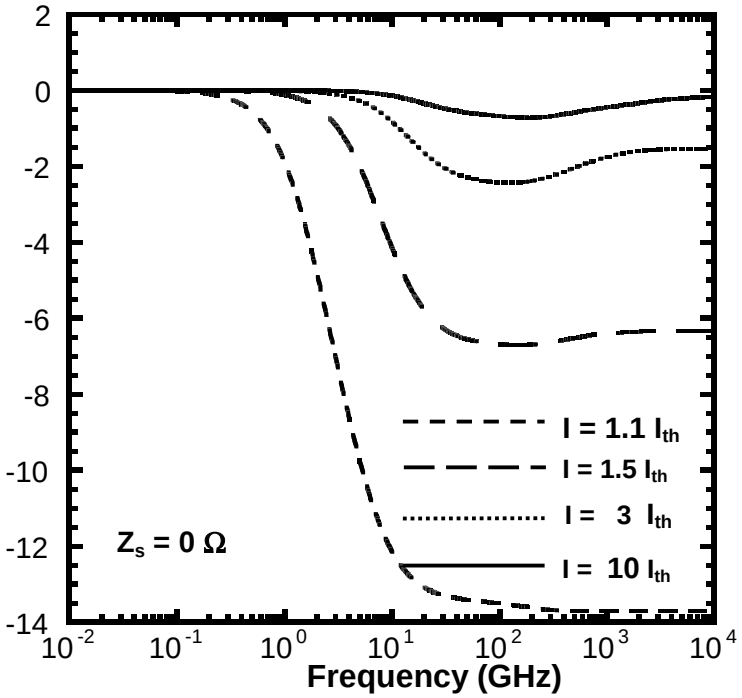

Fig.11: Current noise spectral density (normalized to its value at zero frequency) in the external circuit for different bias currents. The roll-over frequency increases with the bias current as the laser modulation bandwidth increases.

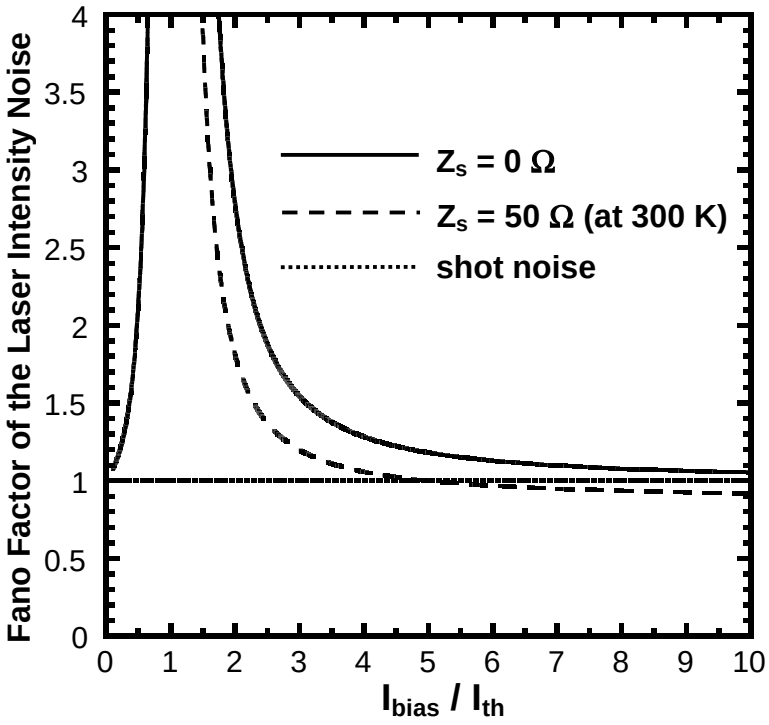

Fig. 12 – Fano Factor of the photon noise for a **QCL.** When the external circuit impedance Zs is large squeezing is observed.

References

1. J. Faist, F. Capasso, C. Sirtori, Appl. Phys. Lett., **66**, 538 (1995).
2. J. Faist, A. Tredicucci, F. Capasso, C. Sirtori, IEEE J. Quantum Electronics, **34**, 336 (1998).
3. C. Gmachl, A. Tredicucci, F. Capasso, Appl. Phys. Lett., **72**, 3130 (1998).
4. C. Sirtori, P. Kruck, S. Barbieri, Appl. Phys. Lett., **73**, 3486 (1998).
5. G. Iannacone, M. Macucci, B. Pellegrini, Phys. Rev. B, **55**, 4539 (1997).
6. Y. M. Blanter, M. Buttiker, Phys. Rev. B, **59**, 10217 (1999).
7. Y. Yamamoto, S. Machida, Phys. Rev. A, **35**, 5114 (1987).

Current Fluctuations in Semiconductor Devices

Sponsor
National Science Foundation
DuPont MIT Alliance

Project Staff
Peter Mayer, Professor Rajeev Ram

Current fluctuations in semiconductors are important for both practical and theoretical reasons. A device's current fluctuations impose a fundamental limit on the best possible signal to noise ratio in a communication or data link. In nearly every system in which information must be extracted out of an analog signal (optical fiber communications systems, modems, cell phones, and A/D and D/A conversion), current noise sets limits on the fundamental sensitivity of the detecting device. In a light emitter such as an LED or a semiconductor laser, current noise in the device is transduced to noise in the emitted photon stream, making current noise a consideration in the design of optical transmitters as well.

The measurement of current fluctuations in semiconductors also provides a window into the internal physical dynamics and correlations of a device. The 3-dB modulation bandwidth of a semiconductor laser can be extracted by examining the dc-biased laser's noise spectrum. Current fluctuation measurements also provide information about the nature of electron transport and dynamics within the device. Coulomb correlations in resonant tunneling diode structures can be inferred from enhanced or suppressed measured current noise.

A suite of techniques for measuring current fluctuations in a variety of devices and operating regimes have been developed. One setup relies on a wide-band microwave measurement of the noise using a calibrated spectrum analyzer and a low noise amplifier. The bandwidth of the system extends into tens of GHz, and the noise floor is set by the background thermal noise of system. To reach noise levels below the 50Ω thermal noise floor, more accurate low-frequency time-domain methods were developed. All measurements must be carefully calibrated to remove the effects of unwanted noise sources in the measurement chain and to account for circuit parasitics. Such careful calibration allows for accurate measurement of device noise down to and below the noise floor of the measurement chain. Fig. 13 shows the results of such a calibration, used to characterize the input referred voltage and current noise of a transimpedance amplifier. Fig. 14 shows the results of a measurement of the shot noise from a photodetector excited by a weakly coupled LED. Another key issue in the measurement of laser and LED current noise is that the low impedance of the light-emitter must be coupled to the high input impedance of the measuring amplifier. A measurement and calibration using a low-noise transformer for impedance matching has been designed to overcome this mismatch.

In the next phase of this research, the noise measurement setups are being used to study various semiconductor lasers, resonant tunneling diodes, and a quantum cascade laser.

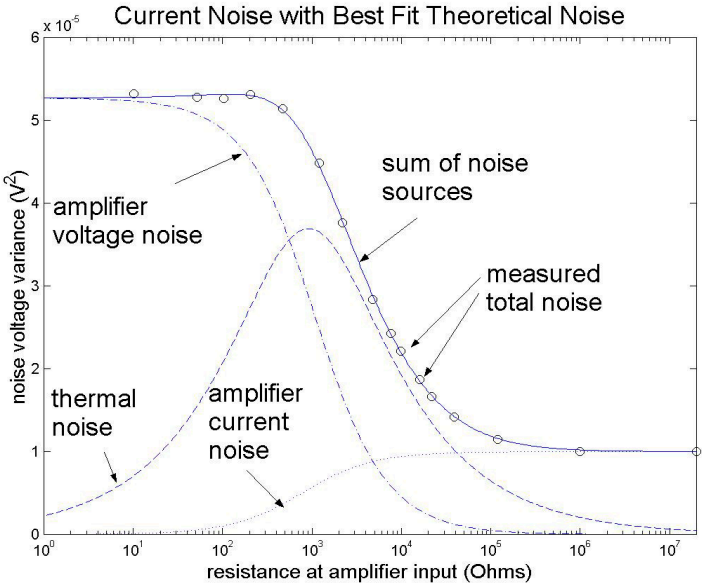

Fig. 13. Fitted and measured transimpedance amplifier noise with varying source impedances.

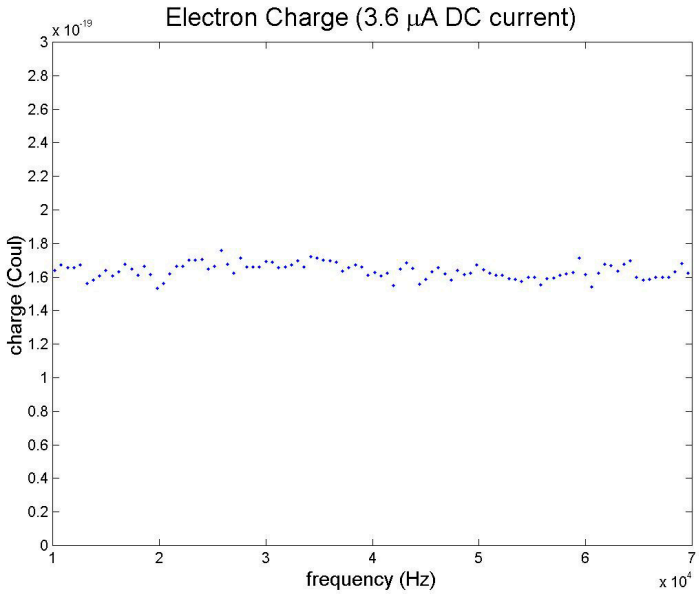

Fig. 14. Charge of electron inferred from photodetector shot noise (a check on noise measurement accuracy).

All-optical wavelength conversion using electromagnetically induced transparency

Sponsor
Office of Naval Research, NEC

Project Staff
Holger Schmidt, Professor Rajeev J. Ram

The transfer of information from one optical wavelength to another is a key element for wavelength routing, data storage, and buffering in wavelength division multiplexing (WDM) communication networks. Wavelength conversion is required for packet switches that connect subnetworks of metropolitan or large local area networks. It can be shown that the load per wavelength channel in the networks can be increased significantly when wavelength conversion is used. All-optical wavelength converters are especially desirable for ultra-high bit-rate operation because they help avoid the intermediate conversion of optical to electronic signals and vice-versa, which acts as a bottleneck on the way to terabit data rates. The most widespread approaches that have been taken to realize all-optical wavelength conversion are based on cross-gain modulation (XGM), cross-phase modulation (XPM), and four-wave mixing (FWM) in semiconductor optical amplifiers (SOA). More recently, cross-absorption modulation (XAM) in electro-absorption modulators and semiconductor intersubband transitions as well as difference-frequency generation (DFG) have been proposed. These schemes rely on the nonlinearity of the conversion medium due to saturation effects (XGM, XPM, XAM) or coherent generation of new wavelengths (FWM,DFG).

We have recently proposed an entirely different method for obtaining wavelength conversion of an optical signal that is based on linear absorption modulation by electromagnetically induced transparency (EIT). EIT is the elimination of resonant absorption of a weak probe field (frequency ω_p, Rabi frequency Ω_p) on an otherwise optically allowed transition by the application of a (strong) coherent coupling light field (ω_c, Ω_c) in a three-level scheme as shown in Figure 15. The atom-field system has a time-independent eigenstate which is a coherent superposition of the atomic states |1> and |2>. This state – also called coherent population trapping (CPT) or dark state - is decoupled from the upper level |3>, thus eliminating absorption of either field.

Figure 16 shows the absorption profile of the probe field applied on the |1>-|3> transition in the absence and presence of the coupling field. At the two-photon resonance (ω_{31}-ω_p=0), absorption cancellation is observed which can be exploited for all-optical wavelength conversion. To this end, the coupling laser is modulated with the signal and the EIT medium is transparent for the cw-probe field only in the presence of the coupling pulse. Due to the fact that EIT relies on quantum interference, the absorption cancellation can be perfect in the absence of dephasing of the dark state coherence, and wavelength conversion with unprecedented extinction ratio is feasible.

In addition, it is well known that EIT can be observed for any pair of fields with vanishing two-photon detuning, i.e. identical detuning from the upper state |3>. We showed that if the dark state of N applied pairs of laser fields is the same, this dark state is a dark state of the entire system and transparency occurs for all applied fields. This situation occurs under two conditions: First, the ratio of the Rabi frequencies of coupling and probe field has to be identical for all applied pairs and secondly, the phase difference between any two probe fields has to equal the phase difference between the respective coupling fields. This opens up the possibility of carrying out NxN wavelength conversion in a single converter simultaneously, albeit only for a set of phase-stabilized fields. This means that (different) bit patterns on N input wavelengths can be converted to N new output wavelengths.

We are investigating the properties and limits of this conversion scheme with special attention to the high frequency regime. Numerical simulations of the propagation dynamics through the EIT medium in the time domain are used to explore the capabilities of the scheme. An example of such a simulation is shown in figure 17 where the coupling pulse (solid line) and the probe field for two values of the coupling

field intensity (dashed and dash-dotted lines) are shown at the output of the EIT medium. We found that the bandwidth of the converter is determined by the preparation time for the dark state, which is observed as a front edge loss of the probe pulse. The bandwidth is proportional to the intensity of the coupling pulse.

The wavelength converter can be realized in a number of systems that exhibit EIT, ranging from atomic vapor such as alkali atoms to solid state systems such as rare earth doped fiber. We are also considering a possible implementation of the converter in semiconductors for the technologically important transition from 1.3 to 1.55 μm. We propose the use of intersubband transitions in the conduction band of an asymmetric double quantum well (ADQW) structure. InGaAs/AlAsSb lattice matched to InP is the most promising material system due to its large conduction band offset, which enables transitions in the 1.55 μm range. The active region of such a structure is shown in figure 18. The three-level scheme is formed by the quantized electronic levels in the two wells and the specific properties such as the amount of wavelength shift can be tailored by bandgap engineering.

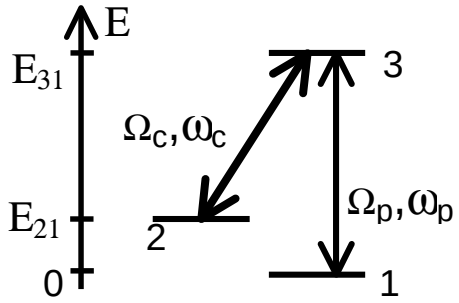

Figure 15

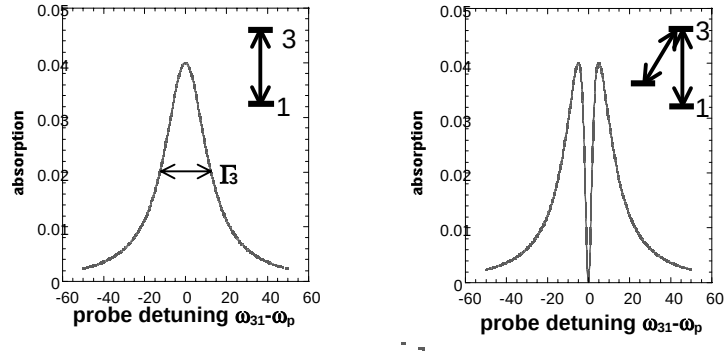

Figure 16

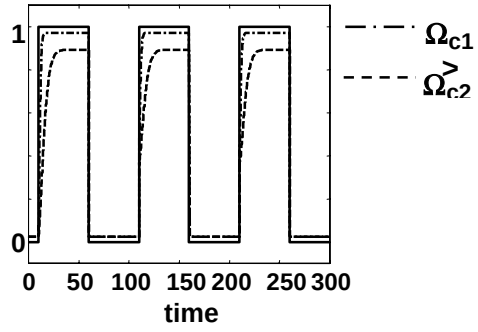

Figure 17

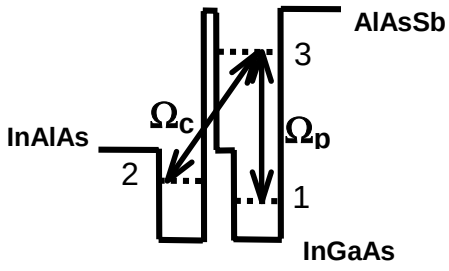

Figure 18

Harmonics in Magnetic Force Microscopy

Sponsor
National Science Foundation

Project Staff
Margaret Wang, Mathew C. Abraham, Professor Rajeev J. Ram

Magnetic force microscopy is a powerful tool for imaging magnetic fields with spatial resolution approaching 10 nm. Deflection of the ferromagnetic-coated cantilever as a function of magnetic sample surface location is used to determine the magnetic field distribution. However, the motion of the elastic cantilever beam interacting with the sample is not easily described. It involves the inclusion of the flexural modes of the beam as well as the interaction forces between the tip and the sample. Furthermore, tip-sample interactions also have the potential of exciting the higher-order flexural modes.

The conventional method used to describe the cantilever motion approximates the deflection at the tip as a damped harmonic oscillator. The resonant frequency of the oscillator is determined by the resonant frequency of the first flexural mode of the beam, and the effective mass and spring constant are chosen accordingly. All higher-order modes are neglected. Hence this model is not sufficient beyond the first-mode.

By examining the transverse motion of an elastic beam, a more complete model can be realized. The beam equation is given by,

$$EI\frac{\partial^4 y}{\partial x^4} + \gamma\rho A\frac{\partial y}{\partial t} + \rho A\frac{\partial^2 y}{\partial t^2} = 0$$

where E is Young's modulus, I is the moment of inertia, γ is the damping term, ρ is the density, and A is the cross-sectional area. In order to solve this equation, boundary conditions at both ends are needed. One end (x=0) is clamped, hence y(x=0) = 0 and $\partial y(x=0)/\partial x = 0$. If the tip-end (x=L) is in the absence of any tip-sample interaction, $\partial^2 y(x=L)/\partial x^2 = 0$ and $\partial^3 y(x=L)/\partial x^3 = 0$. Fig. 19 shows the first four vibrational modes of a freely-vibrating MFM cantilever.

In the presence of magnetic field, the force acting on the tip can be approximated by

$$F = \nabla(\vec{m}\cdot\vec{H})$$

where $\vec{m}$ is the effective magnetic dipole moment of the cantilever tip and $\vec{H}$ is the magnetic field from the sample. This shear force changes the boundary condition at x=L.
From the first-mode approximation, it is shown that the cantilever's amplitude response to magnetic field is proportional to the gradient of the magnetic field. Furthermore, the phase response is given by

$$\Delta\Phi = \frac{Q}{k}(\vec{m}\cdot\nabla^2\vec{H})$$

where Q is the quality factor and k is the effective spring constant. Fig. 20 shows the vertical component of $\vec{H}$, $\nabla\vec{H}$, and $\nabla^2\vec{H}$ as a function of lateral and vertical distance from a 2 *u*m-wide wire carrying 50 mA current.

Comparisons between the first-mode approximation and the flexural-beam model have been carried out. Also, by using the flexural-beam model, a more accurate representation of the photodetection system in MFM is obtained. The optical beam detection system, in reality, measures the cantilever slope at the tip instead of the tip-deflection. The possibility of exciting higher-order modes through the magnetic field generated by an AC-current-carrying wire is also being examined.

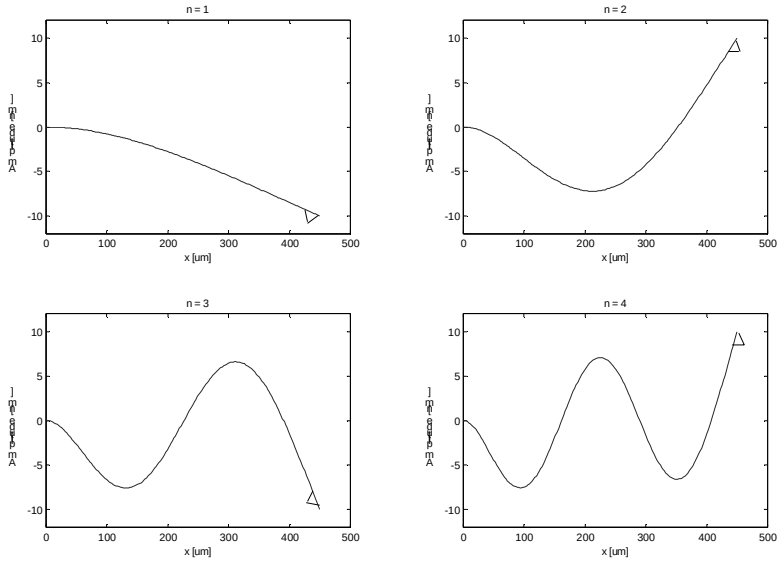

Fig. 19. First four vibrational modes of a freely-vibrating MFM cantilever

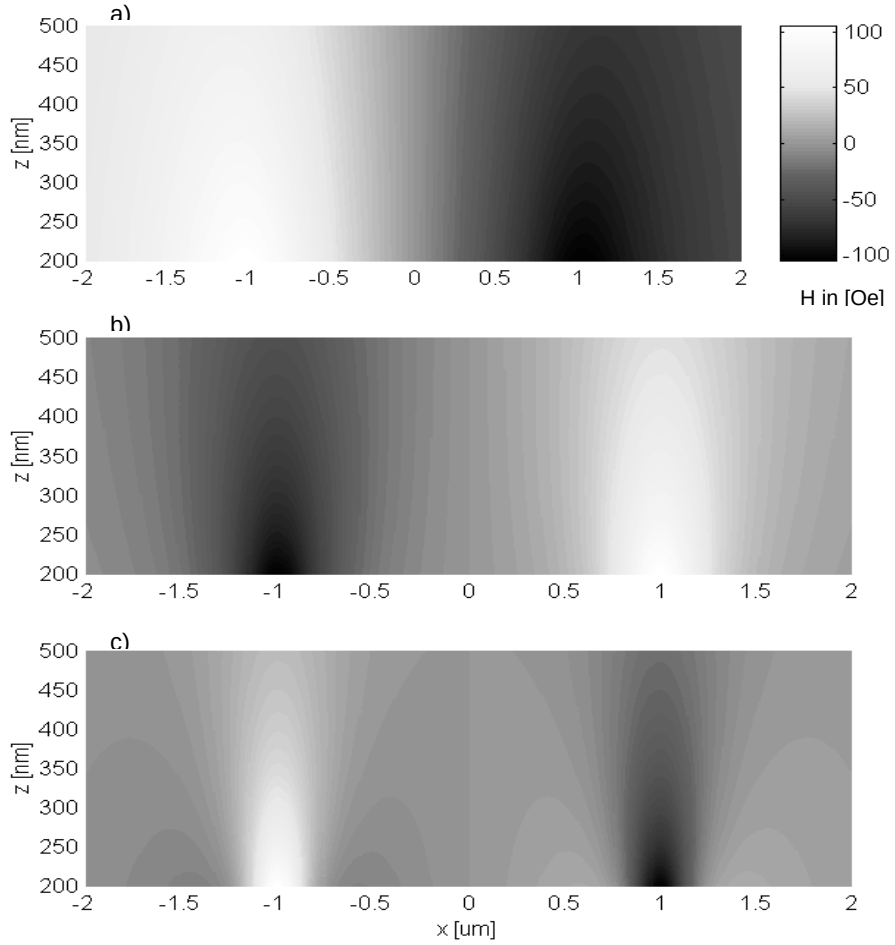

Fig. 20. The vertical component of a) $\vec{H}$, b) $\nabla\vec{H}$, and c) $\nabla^2\vec{H}$ as a function of vertical (z) and lateral (x) distance from the center of a 2*u*m-wide wire carrying 50 mA current.

Magnetic Properties and Interactions of Single-Domain Nanomagnets in Periodic Arrays

Sponsor
National Science Foundation

Project Staff
Mathew C. Abraham, Holger Schmidt, Professor Rajeev J. Ram

Patterned arrays of single domain nanomagnets (SDNMs) have been proposed as candidates for ultra-high-density data storage and ultra-low-power data processing technology. For both applications of SDNMs, the magnetic properties and interaction between nanomagnetic elements must be understood. We made microscopic measurements on a square array of SDNM posts with the magnetic and spatial characteristics that would be desirable for the above applications. Special attention was paid to the interactions between the posts and fluctuations in the magnetic properties of the SDNMs, as these characteristics determine the signal-to-noise ratio in data storage applications and the power loss in magnetic cellular automata circuits.

The sample we studied was a 100 nm period nanomagnetic array. Each element in the array was a single crystal Ni post with an average height of 115 nm and diameter of 57 nm (an SEM of the sample is shown in Figure 21 inset (a)). The average switching field determined by bulk velocity sensitive magnetometry (VSM), was 710 Oe, with an easy axis parallel to the long axis of the post. A microscopic 'hysteresis' curve was measured by taking successive magnetic force microscope (MFM) scans of a fixed 20x20 grid of posts in a varying external magnetic field and recording the switching field of each post. As shown in Figure 21, the microscopic (MFM) and bulk (VSM) data compared well, with a small discrepancy in $^{dm}/_{dH}$ between the two curves. The smaller slope of the VSM curve can be attributed to the fact that the MFM data, part of which is shown in inset (b) and (c), measures just the magnetic state of the post ("up" ↔ white, "down" ↔ black) and not the actual magnetization of each post.

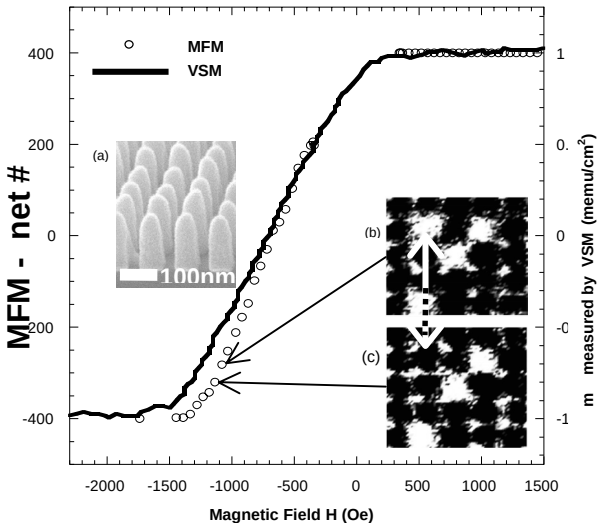

Figure 21: Microscopic (MFM) hysteresis curve compared to bulk (VSM) hysteresis curve. Inset (a) is an SEM image of the magnetic posts. Insets (b) and (c) show a 5X5 section of the MFM data at -1080 Oe and -1136 Oe where one of the posts is seen to have switched its magnetic state from "up" (white) to "down" (black).

The unique information gained from MFM measurements is the microsopic map of the individual switching field. This map gives us the magnetic configuration of the neighboring states as the elements flip. Thus we were able to account for the interaction field of the neighbors in determining the switching field of each element. Figure 22 shows the standard deviation of the average switching field as we account for the interaction fields from 4,8,12,20 and 24 neighbors. The insets in Figure 22 show the distribution of switching fields by taking into consideration (d) no interactions (e) the interactions from 24 nearest neighbors.

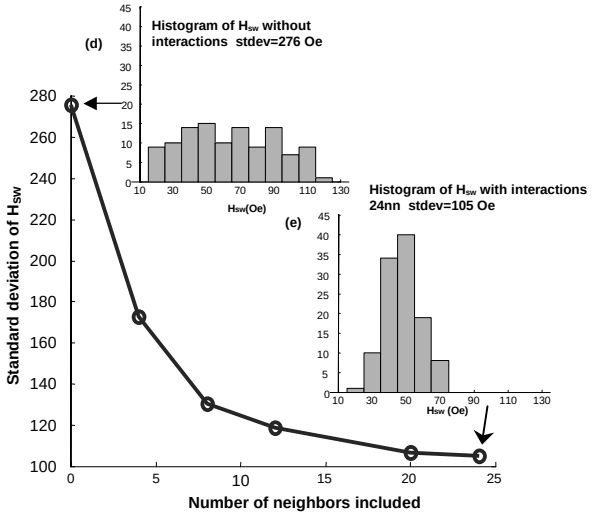

Figure 22: Standard deviation of switching fields vs. number of neighbors included in calculating the switching field. Inset (a) distribution with no nearest neighbor interactions, inset (b) distribution with 24 nearest neighbor interactions.

In addition, simultaneous atomic force microscope (AFM) measurements were made along with the MFM measurements in order to record the size dependence of the switching field. The measured mean switching field, standard deviation and size dependence were accurately reproduced by numerical simulations which assumed the magnetization switching mechanism to be curling.

In summary, we have investigated the switching field behavior of single domain nanomagnets in a dense array. By using magnetic force microscopy, we spatially resolve the hysteresis loops of individual nanomagnets. We showed that magnetostatic interactions play an important role and up to 24 nearest neighbors need to be taken into account to determine the switching field distribution. Also, the experimental features such as mean switching field, standard deviation, and size dependence are well reproduced when curling is assumed as the switching mechanism.

The measurements made so far on the SDNMs were conducted using a room temperature open air scanning probe microscope (SPM). In order to study effects like superparamagnetism, temperature control and improved sensitivity of the MFM is essential. Currently we are in the process of installing a cryogenic high vacuum scanning probe microscope (SPM). The microscope head, shown in Figure 23, is made completely out of non-magnetic materials and has a optical fiber interferometer to measure the deflection of the cantilever. The microscope is designed to operate in STM, AFM contact and AFM non-contact modes over a temperature range of 5K to 300K. The variable temperature range should allow us to study the superparamagnetic transition in SDNMs and also provide greater signal to noise ratio in MFM measurements made at low temperature due to the absence of thermal fluctuations of the cantilever.

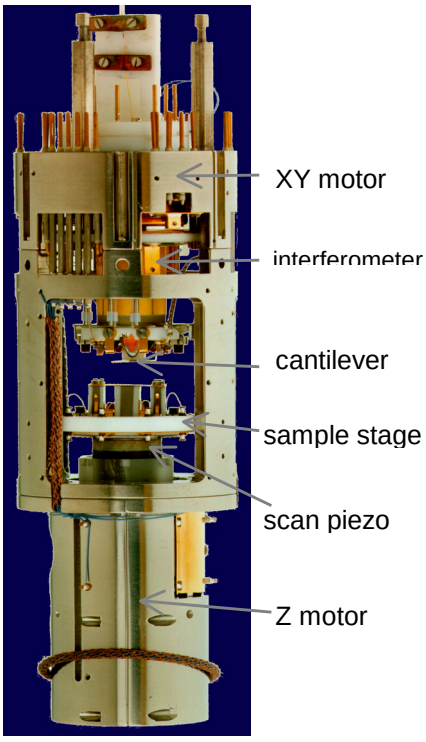

Figure 23: Scanning force microscope head can perform STM, AFM contact and AFM non-contact measurements over a temperature range of 5-300K in high vacuum.

The performance of the cryo-SPM is further enhanced because the high vacuum environment in which the head is placed. The vacuum reduces the damping of the cantilever oscillation thereby substantially increasing the Q of the system and therefore the sensitivity of the measurement. Figure 24 shows a preliminary measurement made in AFM non-contact mode at 5.1K and in high vacuum. The topographic scan is that of a 105nm x 90nm area of a gold film on glass sample. The cross section shows that the instrument is able to resolve monoatomic steps of height 0.27nm.

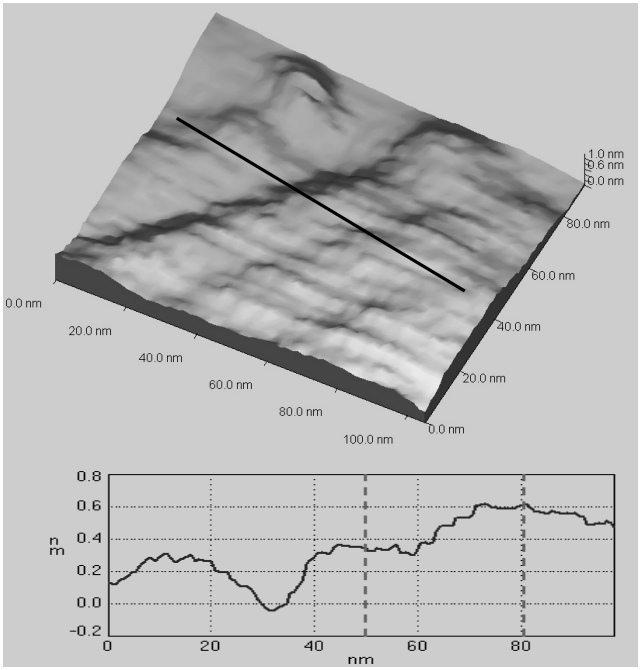

Figure 24: 3D topography of 105nm x 90nm area of a gold film on glass sample measured using cryogenic non-contact AFM. The line profile shows mono-atomic steps measuring 0.27nm. The data was taken at 5.1K and in high vacuum.